Millimetric Inclusion Detection Through a Contactless Microwave Spiral Sensor for Biomedical Applications

Angelica Masi, *Graduate Student Member, IEEE*, Danilo Brizi, *Member, IEEE*, and Agostino Monorchio, *Fellow, IEEE*

***Abstract*—This article introduces the design and fabrication of a microwave contactless sensor used to detect the presence of millimetric inclusions in a biological medium for biomedical applications. The hardware system comprises a self-resonant planar spiral resonator (SR) (sensing element) inductively coupled to an external concentric single-loop probe (reading probe), working at 648 MHz. The microwave sensor configuration relies on the *Q*-factor maximization of the spiral coil, that is, the sensing element, through an optimization process, to obtain a stronger sensitivity and, thus, a millimeter resolution for the inclusions' detection. The detection is achieved by recording both the amplitude variation and the frequency shift of the input impedance of the reading probe. To validate the proposed solution, full-wave simulations have been performed to design and preliminary evaluate the radiating system performance in detecting millimetric biological inclusions. As an applicative example, we focus on air bubbles detection in hemodialysis procedures; in particular, we carried out the experimental verification by employing an agar phantom to replicate the dielectric characteristics of the blood tissue and polylactic acid (PLA) samples of various sizes to represent the air inclusions. We proved that the theoretical assumptions were in excellent agreement with both the numerical and experimental results, encouraging further analysis of the potential use of such sensors in biomedical applications. Indeed, the radiating device can be very helpful for all operations where it is necessary to detect the presence of undesired and dangerous contaminants in a contactless way, making the procedure safer for patients.**

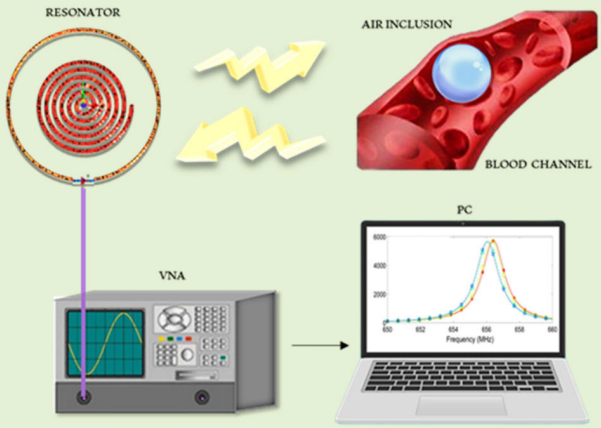

***Index Terms*— Hemodialysis, microwaves, *Q*-factor, sensors, target detection.**

I. Introduction

IN RECENT decades, major medical discoveries have been accomplished, thanks to the evolution of clinical technology. In this context, the demand for biological sensors has increased rapidly. These devices are employed in a wide range of medical equipment, including medical image analysis, portable and clinical diagnostics, and laboratory applications [1], [2]. In agreement with the common definition, biological sensors are electronic devices capable of converting biomedical signals into electrical signals that can be accurately measured [1], [3]. Based on the type of physiological information requested, it is possible to identify four main categories of sensors: physical, chemical, thermal, and biological. The first category also includes sensors for the detection of biological inclusions, which have gained much attention in recent years due to the development of wearable technologies [4].

As a matter of fact, the target to be opportunely detected is represented by an external or undesired object (e.g., molecules and contaminants) that might compromise the patient's health. For instance, lipid accumulations are the target in hypercholesterolemia, as well as blood clots in thrombosis and air bubbles in gas embolism. The latter disease is particularly important and has an increasing incidence due to the rise in the number of dialysis treatments. Indeed,

Manuscript received 3 April 2023; revised 20 April 2023; accepted 20 April 2023. Date of publication 3 May 2023; date of current version 14 June 2023. The associate editor coordinating the review of this article and approving it for publication was Dr. Wensong Wang. *(Corresponding author: Angelica Masi.)*

The authors are with the Department of Information Engineering, University of Pisa, 56122 Pisa, Italy, and also with the Consorzio Nazionale Interuniversitario per le Telecomunicazioni (CNIT), 56124 Pisa, Italy (e-mail: angelica.masi@phd.unipi.it; danilo.brizi@unipi.it; agostino.monorchio@unipi.it).

Digital Object Identifier 10.1109/JSEN.2023.3271412

gas bubbles of various sizes are often produced during the hemodialysis cycle [5]. Clinically, the presence of air bubbles in the bloodstream might be fatal to the patient, causing cardiac arrest or shock [6], [7].

In the literature, a lot of efforts have been directed to develop sensors for target detection in biomedical applications. The earlier developed technology is the optical sensor, which consists of a visible or infrared light source that activated a photoelectric cell on the same or opposite side [8]. The operating principle of an optical sensor is based on the variation of the light refraction and reflection caused by the presence of the target. More specifically, the absence of the target results in a well-defined light path and a standard response from the photocell. Otherwise, the presence of the target causes a change in the photocell's activity, allowing detection [9]. Although they still represent a simple and cost-effective solution, this kind of sensor has significant drawbacks. First, this device is unable to respond if the path of light is obstructed by an obstacle. In addition, the same ambient light could reach the photocell and trigger false alarms; lastly, it is extremely susceptible to external conditions [10].

In [11], another type of target detection sensor has been described, known as a capacitive sensor, which consists of two (or more) capacitors arranged around the target's passage structure. The target is identified by measuring the variation of the capacitive circuit's output voltage. In fact, the presence of the specific target induces changes in the dielectric properties, resulting in a variation of the output voltage. This type of sensor has the potential advantage of being able to detect the target in various media and with an excellent resolution (up to submillimetric inclusion dimensions) [12], [13]. However, as discussed in [14], the transit of the target may result in rapid volume changes, which are followed by a corresponding pressure change that makes the system difficult to utilize and prone to spurious detections. More in detail, the capacity is inversely proportional to the distance between the plates; therefore, it is subject to variation whenever there is a volume change, regardless of the target's presence. A further disadvantage of capacitive sensors is the considerable sensitivity to the external electric field, which has the potential to alter the sensing performance [13], [14].

Currently, the most popular target detection technology is based on ultrasonic sensors. The ultrasonic wave is generated by a transmitting piezoelectric crystal and it is received by a second piezoelectric crystal [12], [15]. As described in [16], the detection principle is based on the variation of the ultrasonic wave's reflection in the presence of the target, which alters the intensity of the signal that reaches the piezoelectric receiver. Ultrasonic detectors are probably the most performant solution currently used in the clinical field. Despite its wide use, several disadvantages are associated with this type of sensor. First, it is necessary to consider that multiple factors may affect the accuracy of target detection, such as the homogeneity of the ultrasonic beam, the quality of the acoustic coupling, and external interferences [14]. Furthermore, the high production costs associated with this technology reduce its accessibility. The last disadvantage of ultrasonic sensors is the footprint, caused by the physical constraint associated with the size of the crystals. For instance, in the specific case of dialysis, the main risk is that the weight of the sensor may cause local damages at the point where it is located and, consequently, hemodynamics may be altered [13].

To overcome the limitations of the current technologies, we propose a microwave sensor for millimetric target detection in biological media for biomedical applications. Although this technology is widely employed in the biomedical field, such as in systems for heating treatments, imaging, dielectric characterization of tissues, and monitoring of biological parameters application [17], [18], [19], to the best of the author's knowledge, microwave technique has never been used for the proposed application. By exploiting microwave radiations, it is possible to perform a contactless measurement of the presence of undesired inclusions in a biological medium.

Although the system is suitable for multiple cases of biomedical target detection, we report a novel sensor design and provide numerical and experimental data to demonstrate the potential feasibility of the particular application of air inclusions detection in hemodialysis systems. Among the various types of microwave resonating sensors, a planar and conformal configuration has been chosen due to its advantages of compact size and easy manufacturing and integration [20]. Indeed, by exploiting printed circuit board (PCB) technology, the proposed sensing system is an affordable and space-saving alternative with respect to the other solutions that appeared in the literature [21]. Furthermore, by leveraging the Q-factor optimization to achieve the best design, it was possible to maximize the sensitivity and the resolution of the system [22]. Hence, for the aforementioned reasons, the advantages of the solution suggested in this article are multiple in terms of cost, placement, and performance. In particular, through an accurate sensor design, it is possible to simultaneously ensure high sensitivity of the system and good penetration depth inside the investigated volume.

The rest of the article is organized as follows. Section II presents the analytical model to describe the operating principle of the sensing system. In Section III, we report the numerical design and characterization of the PCB prototype, while Section IV is devoted to describing and discussing the obtained numerical and experimental results. Finally, the conclusion follows.

II. Analytical Model

As illustrated in Fig. 1(a), the sensing system presented in this article consists of two primary components: a self-resonant microstrip planar spiral coil and an external concentric and coplanar nonresonant single loop probe, inductively coupled [23]. The inner spiral resonator (SR) allows the detection of the inclusion, whereas the external probe has the function of collecting the signal variations. More in detail, as well described in [24], the inner resonator has a subwavelength dimension, that is, the applied electromagnetic (EM) wave has a wavelength that is larger than its physical size. As shown in Fig. 1(b), at the resonant frequency, the SR produces a large electric field in the gap between the loops, which makes this region extremely sensitive to changes

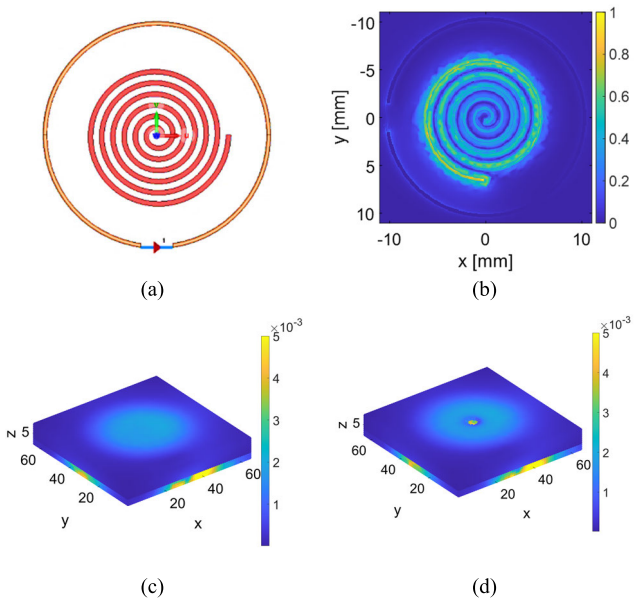

Fig. 1. (a) Front view of the proposed microwave sensing system 3-D CAD. (b) Normalized electric field strength (V/m) over the surface of the structure at 648 MHz. (c) Volumetric electric field distribution (V/m) in the absence of the target within the sensitive region. (d) Volumetric electric field distribution (V/m) in the case of target presence within the sensitive region.

in the dielectric properties of the surrounding medium [25]. Therefore, depending on the presence and EM characteristics of inclusion, the SRs behavior presents a variation that can be quantified by measuring the external probe input impedance (both in amplitude and phase). Fig. 1(c) and (d) depicts the volumetric distribution of the electric field in the analysis domain in the absence and presence of the target, respectively.

In the literature, several works have been carried out to characterize the analytical model of passive SRs [26], [27], [28], [29], [30]. Conventionally, the equivalent circuit of a planar SR can be modeled as an *RLC* series resonator, and these lumped parameters could be accurately determined following the extraction procedure described in [28]. This latter study provides a reliable strategy not only to predict the resonance frequency, but also the behavior of the resonator. It must be considered that the lumped parameters extraction is strictly valid as long as the electrical size of the SR is significantly small with respect to the applied wavelength. It is worth noticing that, in this case, the term resonance refers to the self-resonance of the SR, that is, originated from the intrinsically inductive behavior and the parasitic capacitance, avoiding the use of external lumped reactive elements. Therefore, it is possible to deduce that this feature strongly depends on the geometry of the spiral inductor and the properties of its constituent materials.

The probing loop is fed through a coaxial cable and it is modeled as an inductance in series with a resistance, due to its purely inductive nature. The passive SR positioned nearby is activated via inductive coupling, according to Faraday's law. Basically, the magnetic field generated by the current flowing through the fed circuit induces a secondary current on the passive component by concatenating through the surface of the

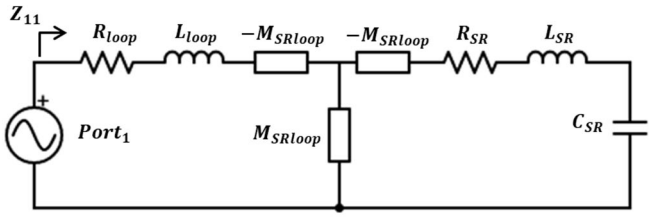

Fig. 2. Schematic of the equivalent lumped circuit for the inductively coupled SR and probe loop.

SR. As a result, there is an energy exchange between the two components [31]. The inductive coupling approach does not require a direct electrical connection to the energized system and therefore it facilitates an on-site integration of the sensing device.

The equivalent circuit of the overall sensing system is depicted in Fig. 2. In this model, R_{SR} represents the metal trace resistance, L_{SR} the inductance, and C_{SR} the parasitic capacitance for the SR, whereas the external probe loop is schematized by R_{loop} and L_{loop} due to its purely inductive behavior. The mutual coupling between the two main components is taken into consideration by the coupling coefficient M_{loopSR}.

Given the voltage on the probing loop V_1, by exploiting the frequency domain, it is possible to express Kirchhoff's equations in the following form:

$$\begin{cases} \left(R_{\mathrm{loop}} + j\omega L_{\mathrm{loop}}\right) I_1 + j\omega M_{\mathrm{loopSR}} I_2 = V_1 \\ \left(R_{\mathrm{SR}} + j\omega L_{\mathrm{SR}} + \dfrac{1}{j\omega C_{\mathrm{SR}}}\right) I_2 + j\omega M_{\mathrm{loopSR}} I_1 = 0. \end{cases} \tag{1}$$

Therefore, through simple algebraic manipulations, the input impedance can be defined as

$$Z_{\mathrm{input}}(\omega) = \frac{V_1}{I_1}$$

$$Z_{\mathrm{input}}(\omega) = R_{\mathrm{loop}} + j\omega L_{\mathrm{loop}} + \frac{\omega^2 M_{\mathrm{loopSR}}^2}{R_{\mathrm{SR}} + j\omega L_{\mathrm{SR}} + \frac{1}{j\omega C_{\mathrm{SR}}}}. \tag{2}$$

The presented sensing system performs the target detection inside the surrounding biological medium by capturing the resonant frequency shift and the peak variation of the input impedance amplitude. Indeed, as previously mentioned, the overall dielectric characteristics vary when the target is present inside the sensitive region, mainly influencing the SR response.

As anticipated, the physical principle at the basis of the proposed method consists of the interactions between the radiating system and biological tissues. Indeed, it is well known that the EM properties of a medium are substantially determined by the interactions of polar molecules and ions with the electric field. For biological tissues, such interactions are mainly due to the water content, which is the main component [32]. Therefore, due to their different compositions, each tissue is characterized by specific dielectric properties, quantifiable by the relative permittivity, ε_r, and

the electrical conductivity, σ (S/m). With regard to magnetic permeability μ_r, as profusely demonstrated in the literature, biological tissues can be considered nonmagnetic [33].

Owing to the dissipative behavior exhibited by biological tissues, relative permittivity has two components: a real and an imaginary part, as

$$\varepsilon_r = \varepsilon_r' - j\varepsilon_r''. \tag{3}$$

The real part describes the material's capability to store electric field energy, whereas the imaginary part describes the loss due to heat dissipation. These parameters are frequency-dependent according to the physical mechanisms excited inside the material; indeed, biological tissues are intrinsically dispersive media [34], [35]. The loss component can be linked to the electrical conductivity σ

$$\varepsilon_r'' = \frac{\sigma}{\varepsilon_0 \omega} \tag{4}$$

where ε_0 is the dielectric permittivity of the vacuum.

In view of the foregoing considerations, the interaction of biological tissues with EM radiation gives rise to three main effects. First, polarization effects occur, related to the dielectric behavior of the biological tissue. Indeed, the total electric field in a dielectric material is the sum of the applied and the induced electric field, which is the result of the material polarization. Second, electric conduction currents are generated, proportionally with the conductivity value of the considered tissue. Lastly, as has been demonstrated in recent numerical and experimental studies [36], [37], when a conductive biological tissue is invested by a time-varying EM field, eddy currents are also induced, altering the initial EM field. The induction of currents is extremely important in numerous biomedical applications, for example, in magnetic resonance imaging (MRI) systems [38], transcranial magnetic stimulation (TMS) [39], and magnetic hyperthermia [40].

As a result, it is possible to include the above-mentioned effects of the surrounding medium properties on the radiating systems in terms of equivalent circuits (2). Exploiting the procedure described in [28], we can analytically link the circuital lumped parameters with the variations in ε_r' and ε_r''. In particular, the complex dielectric permittivity is going to multiplicate the capacitive free space term C_{SR} in (2) [41]. More in detail, the equivalent complex permittivity values can be estimated by using the Maxwell–Garnett formula, taking into account the presence of the biological tissue and the target of interest. As an example, we herein report different cases, considering an increasing dimension of air inclusion in a fixed volume of blood

$$\varepsilon_{\text{eff}} = \varepsilon_{\text{blood}} + 3\eta\varepsilon_{\text{blood}} \frac{\varepsilon_{\text{air}} - \varepsilon_{\text{blood}}}{\varepsilon_{\text{air}} + 2\varepsilon_{\text{blood}} - \eta(\varepsilon_{\text{air}} - \varepsilon_{\text{blood}})}. \tag{5}$$

In the previous relation, η is the volumetric fraction of the inclusion in the mixture, while $\varepsilon_{\text{blood}}$ and ε_{air} are the complex permittivity of blood and air, respectively. Finally, ε_{eff} is the total effective permittivity. The reader can find further details in [42]. The real part of the complex permittivity and conductivity values for different blood and air mixture are shown in Table I.

TABLE I
EFFECTIVE DIELECTRIC CONSTANT AND CONDUCTIVITY OF BLOOD–AIR MIXED SOLUTION AT 648 MHZ

Air fraction η (%)	*Air inclusion diameter (mm)*	ε_r'	*σ (S/m)*
0	-	62.39	1.43
3.5	5.30	59.26	1.36
7.0	6.80	56.15	1.29
11.0	7.80	53.03	1.22
14.5	8.60	49.91	1.15
19.0	9.40	46.79	1.07

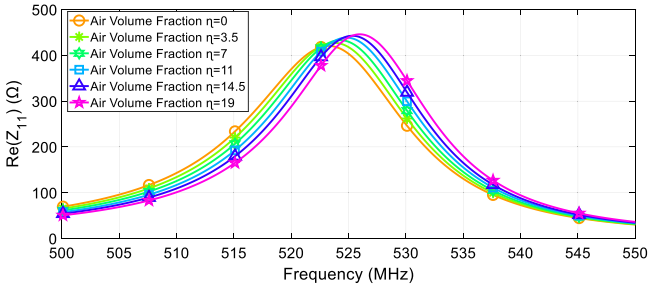

Fig. 3. Probe loop input impedance behavior for increasing fractions of air within the blood volume. The real part is increasing its maximum peak value as the air fraction increases with a corresponding resonant frequency shift towards higher frequencies.

Clearly, as the air content increases within the volume of analysis, the percentage of water and electrolytes decreases [43]. Consequently, both the relative dielectric permittivity and conductivity decrease. Therefore, as the fraction of air grows, the real part of the input impedance undergoes a progressive increase in its maximum peak and a resonance shift to higher frequencies, as shown in Fig. 3 and as predicted by (2).

III. DESIGN PROCEDURE

A. Numerical Design

The numerical design has been carried out by exploiting the EM simulation software CST STUDIO SUITE[1] (CST Studio Suite, Dassault, France). As mentioned previously, the sensing coil consists of a multiturn planar SR, while the probing loop is a simple single-turn structure.

To obtain the optimal SR geometry for our application, one of the most important parameters consists of its quality factor. According to the formal definition, the Q-factor is the total energy absorbed by the resonator divided by the energy lost per cycle ($Q = E/\Delta E$), which can be optimized either by increasing the absorbed energy or by minimizing the losses [44]. Basically, this means that the higher the value of the Q-factor, the greater the contribution of stored reactive energy over the losses. Since the stored energy is primarily responsible for the inclusion detection, it can be inferred that an optimized Q-factor will lead to a more sensitive system.

To carry out an optimized design of the sensing device for our specific application, the first point was to maximize

[1]Registered trademark.

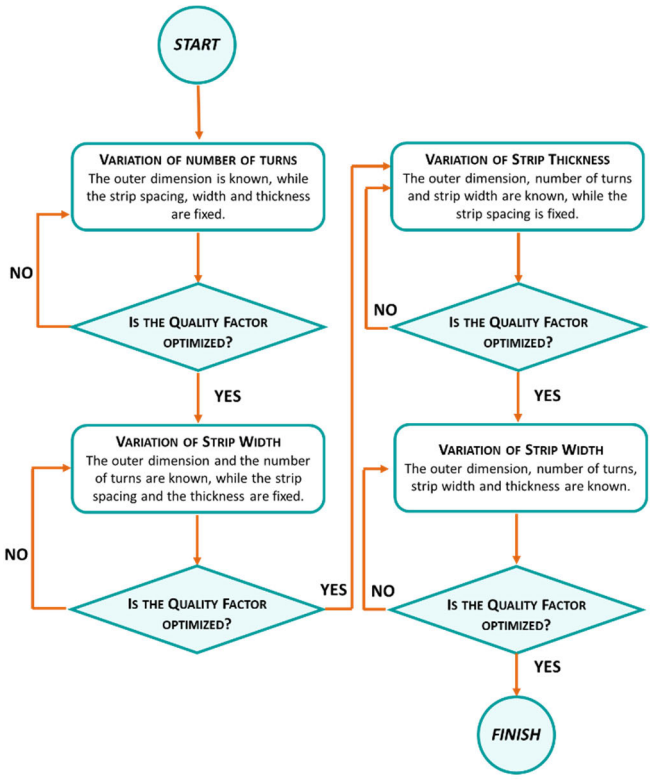

Fig. 4. Flowchart summarizing the main steps for achieving the best geometry of the sensor.

the SR's area. Since our target applicative example is a hemodialysis procedure, we dimensioned the SR's external diameter to be equal to the maximum size allowed, which corresponds to the circumference of a typical 6-mm diameter catheter. Naturally, the SR size could differ according to the particular application specifications. Moreover, the adopted detecting system's operating frequency was selected as 648 MHz. This frequency ensures both a high-quality factor and a good level of system miniaturization. All the system components were designed by adopting a lossy copper microstrip. Conversely, the probing loop was conceived as a single-turn loop with an external diameter of 28 mm.

At this point, once the external dimensions of the SR have been selected, the quality factor was optimized. Several studies have been conducted to determine how the resonator geometric parameters affect its performance [45], [46]. It is worth highlighting that for an RLC circuit, as in the current case, the Q-factor can also be calculated as follows:

$$Q_F = \left.\frac{\omega L}{R}\right|_{\omega=\omega_0} \tag{6}$$

where ω_0 is the resonant frequency. Therefore, we implemented the approach described in [28] to find the highest Q-factor configuration. The main geometric characteristics of a microstrip SR have been evaluated: the number of turns, strip width, strip thickness, and the gap between two consecutive turns. The flowchart in Fig. 4 summarizes the major steps for identifying the optimal geometry of the sensor.

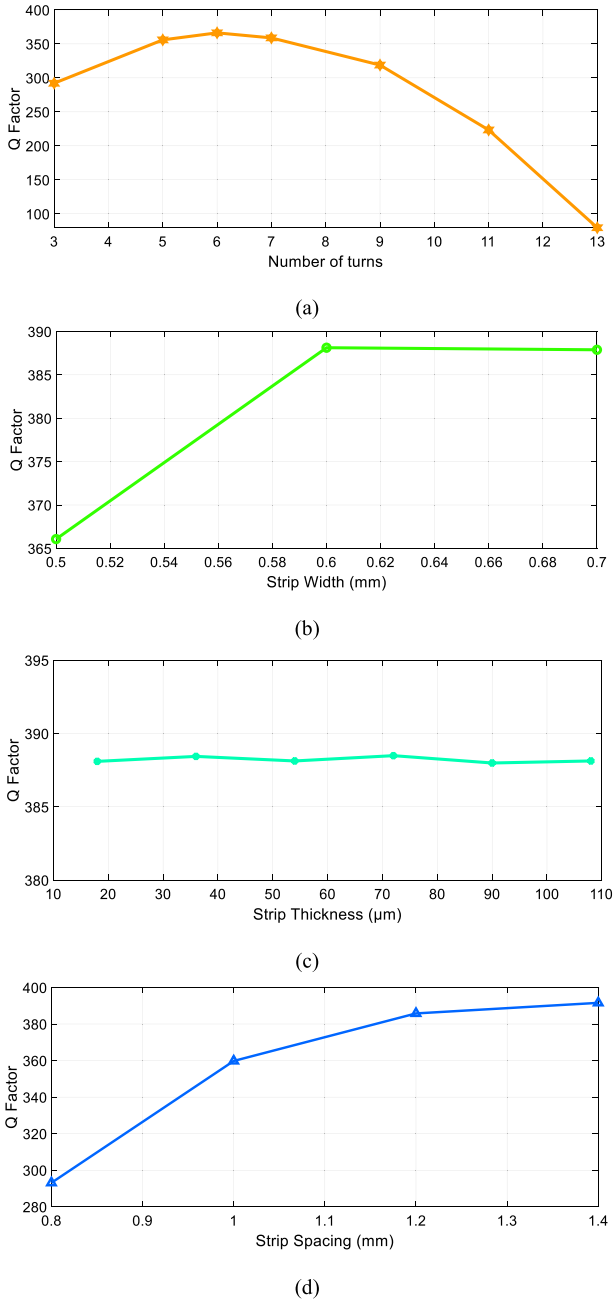

Fig. 5. Evaluation of the quality factor as a function of: (a) number of SR windings; (b) strip width; (c) strip thickness; and (d) strip spacing.

The behavior of the quality factor in relation to each of these characteristics is shown in Fig. 5(a)–(d), respectively. In each graph, it is possible to identify the optimal value of the corresponding geometric characteristic which leads to the maximum Q-factor value. Thus, following the optimization process, an SR design with a Q-factor of about 391 was obtained, which is a considerable value for a microstrip planar structure [47], [48], [49].

A multiturn structure with a number of six windings and a winding pitch of 1.4 mm has been identified as the best SR design. It is important to keep in mind that the quality factor, as depicted in Fig. 5(c), is essentially independent of the microstrip's thickness. As a result, this parameter was selected

TABLE II
SYSTEM DESIGN PARAMETERS

Parameters	*Probing loop*	*Sensing SR*
Outer diameter	13.7	18 mm
Inner diameter	6.7	1.2 mm
Number of turns	1	6
Strip width	0.6 mm	0.6 mm
Strip thickness	35 µm	35 µm
Strip spacing	N/A	1.4 mm

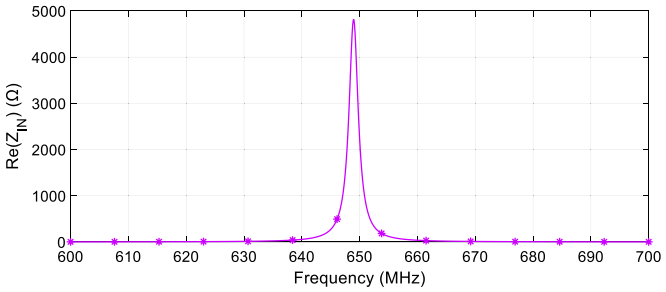

Fig. 6. Real part of the probe loop input impedance as a function of the frequency. The operating frequency of the system is approximately 648 MHz.

as the conventional standard thickness for PCB technology, that is, 35 μm. Table II reports all of the proposed design's geometrical features.

Once the final sensing geometry was identified [as reported in Fig. 1(a)], we first assessed the system response in the stand-alone configuration, that is, without any biological medium placed in the sensing device nearby. By analyzing the probe loop input impedance behavior (reported in Fig. 6), it is possible to clearly observe the inner SR resonance at 648 MHz, confirming the reliability of the design process.

B. Prototype Fabrication

PCB technology was selected for the realization of the prototype due to its benefits in terms of cost, ease of fabrication, large-scale production, and electronic integration. In addition, by exploiting this manufacturing process, it is possible to obtain prototypes with good mechanical properties and excellent repeatability [50].

By following the geometrical constraints from the design process, we used, for the probing loop prototype, a 0.8-mm-thick FR4 ($\varepsilon_r = 4.3, \delta = 0.025$) substrate with 35-$\mu$m-thick and 1-mm-wide copper strips etched on the top layer [refer to Fig. 7(a)]. On the other hand, the sensor substrate [whose prototype is represented in Fig. 7(b)] has been made of FR4 with a lower thickness substrate, equal to 100 μm, to ensure both mechanical strength and excellent bending capability, as illustrated in Fig. 7(c). This feature is fundamental for realizing a conformal sensor with respect to the chosen structure, in our case a catheter. To provide an understanding of the sensor prototype dimension, Fig. 7(d) shows the comparison with a commonly used object. Naturally, as it was discussed for the numerical design, no external capacity was included in the prototype design.

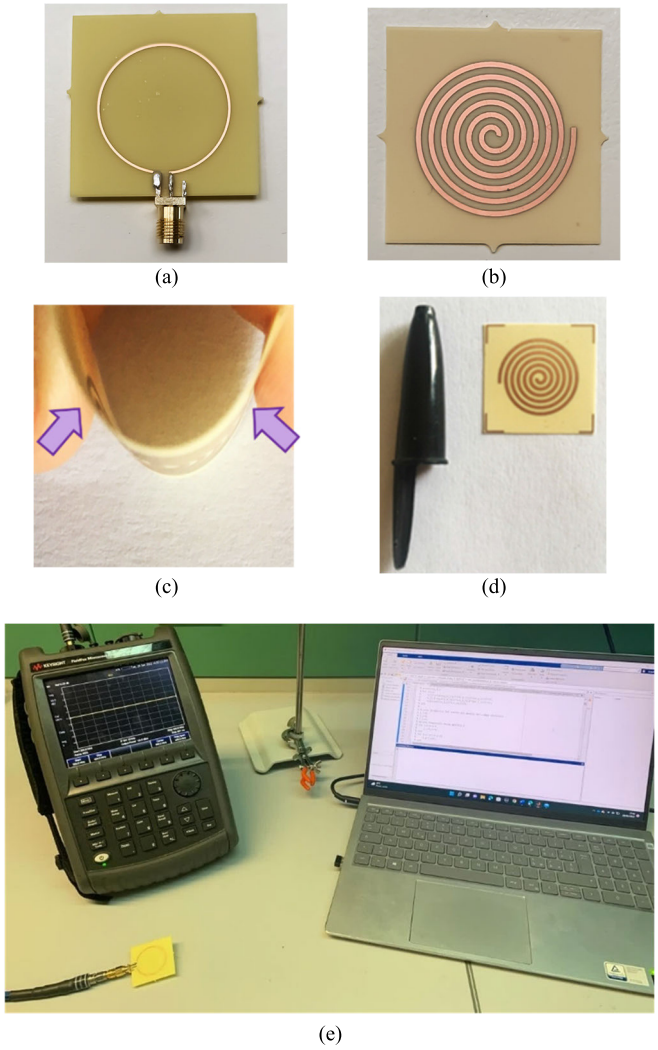

Fig. 7. Representation of experimental prototypes and setup: (a) probing loop's PCB; (b) SR PCB; (c) bending test for SR PCB; (d) comparison of the size of the SR PCB with an object of common use, underlining the good miniaturization of the system; and (e) experimental measurement setup, which includes also VNA and PC laptop.

Finally, we connected the probing loop to a vector network analyzer (VNA) (VNA P9374A, 300 kHz–20 GHz, Keysight, USA) by using a subminiature version A (SMA) PCB connector soldered to it. The instrumentation for the experimental measurements is reported in Fig. 7(e).

IV. RESULTS AND DISCUSSION

A. Numerical Results

To verify our methodology, we carried out full-wave simulations, exploiting an EM solver based on the finite-element method (CST Studio Suite). Therefore, we implemented a simplified, but representative, numerical model, which included the microwave sensor [the 3-D CAD is shown

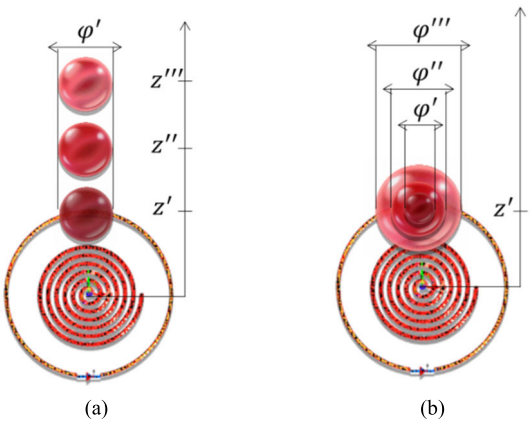

Fig. 8. Two simulated scenarios were conceived to evaluate the designed sensor performance. (a) Increasing relative distance by maintaining the same inclusion size. (b) Increasing the size of the spherical blood inclusion for a fixed distance from the sensor.

in Fig. 1(a)] and, 1 mm above it, a small spherical inclusion with blood dielectric properties, simulating a small target to be detected [51]. This basic model allows us to reduce the complexity of the geometry and, consequently, avoid incurring numerical issues associated with the tiny size of the target. The values of the dielectric properties used for the biological tissue are reported in the first row of Table I. This setup allows us to evaluate the resolution capability of our sensing design in spotting small details, without recurring to high-demanding simulations from a computational cost point of view.

In particular, to evaluate the system sensing performance, two different scenarios have been simulated. In the first configuration [see Fig. 8(a)], the system response in the presence of inclusion with a fixed size and an increasing relative distance from the sensor was studied. Conversely, in the second numerical case, depicted in Fig. 8(b), we fixed the relative distance between the sensor and the inclusion, but varying its diameter.

In Fig. 9(a), we assessed the sensor response by changing the distance between the radiating system and the inclusion (with a fixed diameter equal to 1.7 mm), from 2 to 4 mm. As expected, by increasing the relative distance, the input impedance of the probe showed a proportional amplitude variation and a frequency shift toward the case with the absence of the inclusion. According to the above-mentioned theoretical concepts, as long as the relative distance increases, the target is correspondingly moving away from the near-field region, resulting in an attenuation of the EM field produced by the sensor and, therefore, in detecting effectiveness degradation.

In the second case study, whose results have been reported in Fig. 9(b), we evaluated the sensor response as a function of the blood spherical inclusion dimension (from 0.6 to 0.85 mm). Basically, we observed a progressive downshift in the operating frequency and a proportional amplitude reduction with respect to the baseline case (i.e., absence of target), for increasing inclusion size. Even in this case, the behavior is coherent with the physical concept, as the

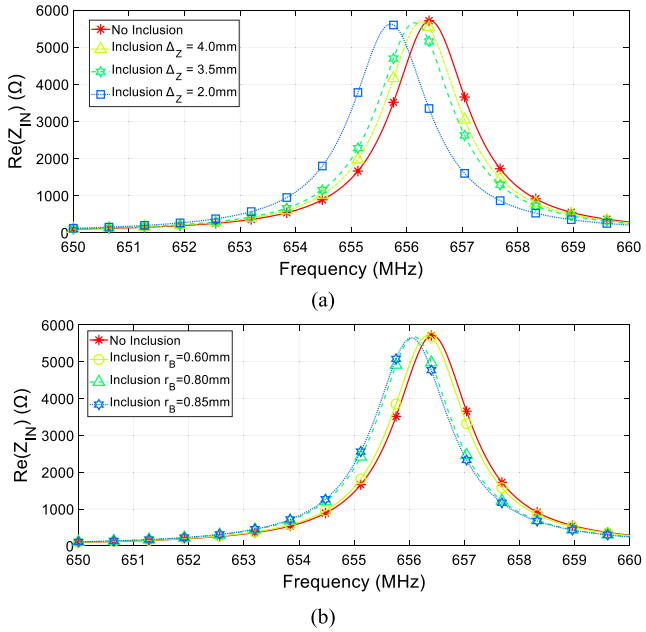

Fig. 9. System response following the two investigated numerical scenarios. (a) Real part of the system input impedance as a function of different inclusion distances (fixing the inclusion dimension). (b) Real part of the system input impedance against inclusion dimensions.

TABLE III
RESONANCE FREQUENCY AND MAXIMUM AMPLITUDE VARIATION OF THE PROBING LOOP'S INPUT IMPEDANCE, SIMULATED FOR THE FIRST CASE STUDY AGAINST THE BASELINE

Inclusion Relative distance (mm)	Δf (%)	ΔZ (%)
2.0	-0.11	-1.69
3.5	-0.04	-1.04
4.0	-0.02	-0.59

TABLE IV
RESONANCE FREQUENCY AND MAXIMUM AMPLITUDE VARIATION OF THE PROBING LOOP'S INPUT IMPEDANCE, SIMULATED FOR THE SECOND CASE STUDY AGAINST THE BASELINE

Inclusion radius (mm)	Δf (%)	ΔZ (%)
0.60	-0.01	-0.18
0.80	-0.05	-0.73
0.85	-0.06	-1.19

presence of the inclusion enhances the equivalent dielectric permittivity and conductivity values experienced by the sensor. Tables III and IV report the percentage variations of the resonance frequency and of the maximum amplitude of the probing loop's input impedance, respectively, measured for different SR-inclusion relative distances and for different inclusion sizes involved in the two numerical scenarios. These percentage levels are calculated against the baseline case (i.e., absence of target).

B. Experimental Results

As the last step, we experimentally tested the sensing performance of our prototype, in accordance with the analytical model and the numerical simulations previously presented.

To conceive a practical scenario, we selected the detection of a small inclusion within a catheter, similar to the air bubble detection task in hemodialysis procedures. Due to ease of availability, the catheter was simply represented by a commercial syringe, presenting a volume of 5 ml. Second, the biological phantom that mimicked blood tissue was created by diluting agar (E406) in water with a concentration of 2% w/v, using the syringe as a container. At this point, to test the response of the system in the presence of increasing size inclusions, it would have been required to fabricate and inject in the syringe dimensionally controlled air bubbles. Nevertheless, as it is well known in the literature, the creation of time-stable and dimensionally controlled air bubbles is a really challenging task [52], [53]. Therefore, to recreate stable inclusions, we make use of polylactic acid (PLA) spheres made by 3-D printing [Anycubic I3 Mega, represented in Fig. 10(a)]. Fig. 10(b), instead, shows the PLA inclusions obtained through the 3-D printing process. In particular, PLA has been selected as the inclusion material because it represents a good compromise between machinability in small samples and a dielectric permittivity comparable to that of air (since it is a plastic material, $\varepsilon_r = 2.75$ [54]). Lastly, the PLA spheres were precisely positioned in each biological sample [see Fig. 10(c)] and the sensing prototype was bent on the syringe by employing a digital caliper, to set an equal distance between the sensor and the base of the syringe for each sample [see Fig. 10(d)]. We employed biological samples containing inclusions of sizes 0.4, 0.6, 0.8, 1, 1.7, 2, and 3 mm, respectively. The final experimental setup is depicted in Fig. 10(e). The biological sample, equipped with the sensor, was positioned and firmly attached to the holder. We performed the measurement by placing the probing loop above the sample, fixing it stably to the support, and connecting it to the VNA. It is noteworthy to mention that, in this preliminary experimental stage, the probing loop was positioned in contact with the resonator to avoid measurement errors due to the placement. Future studies will analyze how the reading-sensor relative arrangement affects the outcomes and how this uncertainty source might be minimized, such as by the use of convolutional neural network approaches [55], [56].

Conversely, Fig. 11 shows the obtained experimental results. In particular, as evident from Fig. 11(a), we observed a significant upshift of the sensor resonance frequency and a general trend showing the maximum peak growth of the real part of the probe loop input impedance for increasing dimension inclusions. Therefore, as also discussed for the numerical results, the experimental outcomes demonstrate a good agreement with the theoretical principle. Indeed, the presence of the PLA inclusion within the biological phantom produces a decrease in the equivalent permittivity and conductivity. Specifically, the larger the size of the inclusion, the stronger the input impedance variation (both in terms of

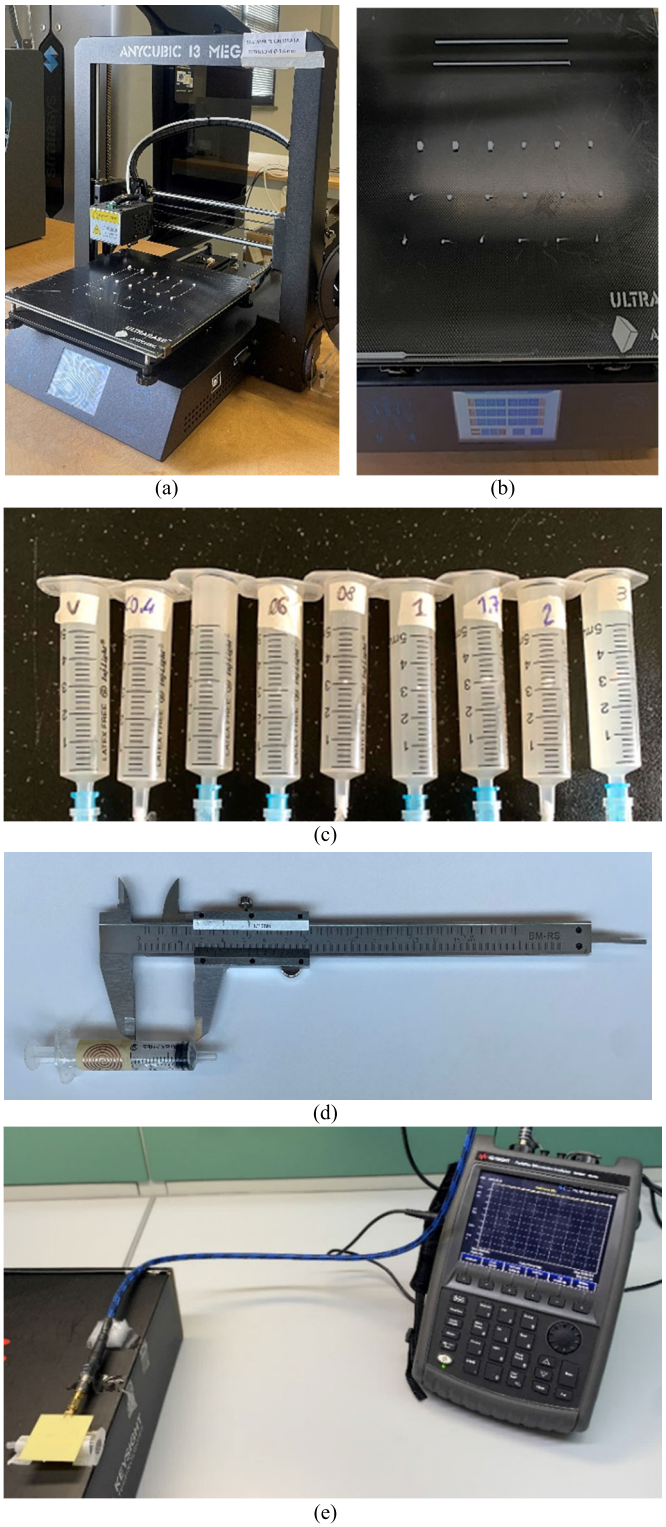

Fig. 10. (a) Anycubic I3 Mega 3-D printer used for the realization of PLA inclusions. (b) Printing process of PLA inclusions. (c) Final biological samples containing PLA inclusions. (d) Sensor placement around the syringe surface, exploiting a digital caliper. (e) Final experimental setup, including the sample under test (placed on the black support), above which is positioned the probing loop's PCB, connected to the VNA.

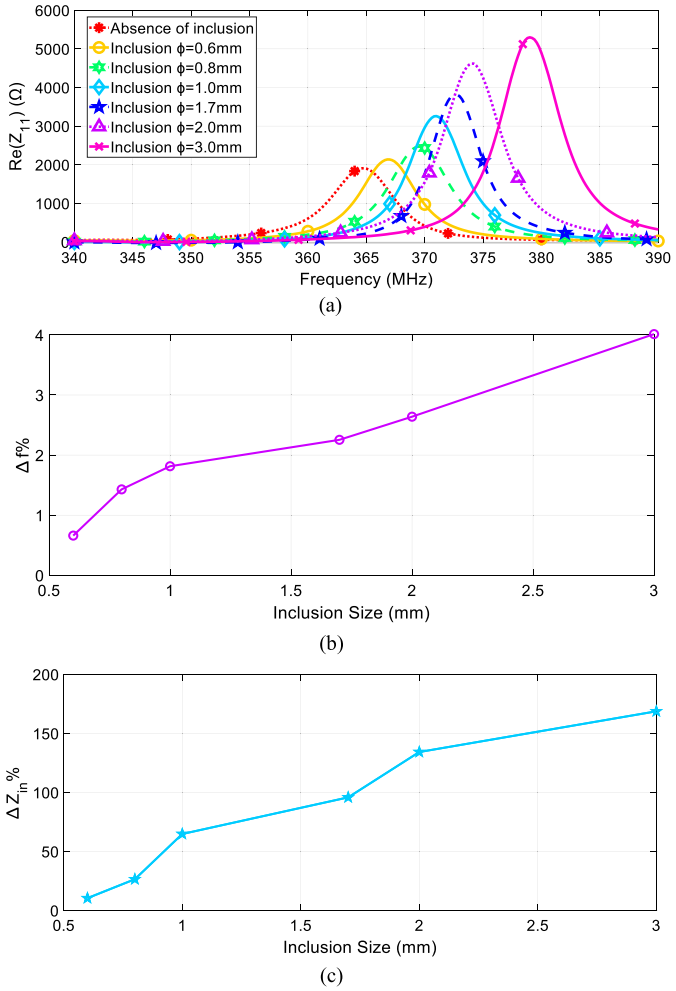

Fig. 11. (a) Real part of the probe loop input impedance as a function of frequency for different inclusion dimensions (reported in legend). The baseline case is represented by the red star line. (b) Resonant frequency shift percentage variation with respect to the baseline case. (c) Percentage variation of the probe loop input impedance (maximum value of the real component) with respect to the baseline case.

TABLE V
STATISTICAL PARAMETERS RELATED TO THE RESONANCE FREQUENCY FOR DIFFERENT INCLUSION SIZES, USED FOR EVALUATING SENSOR PERFORMANCE

Inclusion radius (mm)	*Mean Value (MHz)*	*Mean Relative Error*	*Standard Deviation (MHz)*	*Sensitivity (MHz/mm)*
0.00	363.29	1.70	0.178	-
0.60	366.80	1.20	0.124	3.33
0.80	369.60	0.89	0.104	14.00
1.00	369.56	0.65	0.084	7.00
1.70	372.60	0.98	0.109	2.28
2.00	374.65	0.22	0.026	4.67
3.00	379.72	1.30	0.128	5.00

TABLE VI
STATISTICAL PARAMETERS RELATED TO THE MAXIMUM AMPLITUDE VARIATION OF THE PROBING LOOP'S INPUT IMPEDANCE FOR DIFFERENT INCLUSION SIZES, USED FOR EVALUATING SENSOR PERFORMANCE

Inclusion radius (mm)	*Mean Value (kΩ)*	*Mean Relative Error*	*Standard Deviation (Ω)*	*Sensitivity (Ω/mm)*
0.00	1.90	0.020	15.85	-
0.60	2.14	0.018	14.11	378.47
0.80	2.47	0.010	8.37	1676.0
1.00	3.26	0.013	14.34	3934.1
1.70	3.82	0.035	47.54	807.46
2.00	4.62	0.019	18.37	2650.0
3.00	5.30	0.021	23.50	679.25

frequency shift and impedance value). It is worth noticing that an overestimation of the results in the case of the 0.6 and 2 mm inclusions may have occurred due to errors in the PLA sample positioning.

In addition, Fig. 11(b) and (c) reports the percentage variations in terms of resonance frequency shift and maximum peak of the probe loop input impedance (real component) with respect to the baseline (i.e., absence of any inclusion). By means of this representation, it is easier to quantify the variations of the control parameters. In particular, evaluating the graph of the input impedance percentage variation, it can be worth underlining that a percentage change in terms of real impedance greater than 1%, which can be appreciated by common reading systems such as the VNA, is observed for any PLA inclusion. Therefore, the excellent resolution of our microwave sensor is proved. In Tables V and VI, different statistical parameters derived by collecting a sufficient number of measurements (20 measures for each inclusion size) for both the control parameters are presented. In particular, after calculating the mean value of each dataset for every inclusion size, we evaluated the mean relative error (MRE), standard deviation (SD), and sensitivity (S) of the measurements, as suggested in [57], [58], and [59]. The relations used to calculate the mentioned statistical parameters are detailed below

$$\mathrm{MRE} = \frac{1}{n\bar{Y}} \sum_{i=1}^{n} \left| Y_i - \bar{Y} \right| \tag{7}$$

$$\mathrm{SD} = \sqrt{\frac{\sum_{i=1}^{n} (Y_i - \bar{Y})^2}{(n-1)}} \tag{8}$$

$$S = \frac{\partial y}{\partial x}. \tag{9}$$

Clearly, additional work must be conducted to ameliorate the stability of the measurements and to obtain a more reliable experimental setup. To summarize and have a better insight into the performance of microwave sensors for nondestructive sensing, a comparison between the solution described in this work and the state-of-art permittivity detection sensors is reported in Table VII.

TABLE VII
COMPARISON OF MICROWAVE SENSORS FOR NONDESTRUCTIVE PERMITTIVITY DETECTION

Ref	*Active Components Used*	*Sensor Structure*	*Sensing Method*	*Resonance Frequency*	*Penetration Depth at σ=1 S/m [mm]*	*Quality Factor*	*Sensitivity*	*Minimum Detectable Variation*
[60]	Yes	Planar SRR resonator	Q_F and f_R	2.08 GHz	11.0	105800	-	2.5% of ε_r
[61]	Yes	Planar SRR resonator	Q_F and f_R	1.55 GHz	12.8	15400	-	0.1 ppb of ε_r
[62]	No	SIW cavity resonator	f_R	3.16 GHz	9.0	-	52 MHz/ε_R	-
[63]	No	SRs and SSPP TL	$\lvert S_{21}\rvert$ and f_R	8.13 GHz	5.6	214	2458 Hz/ε_R	-
[64]	No	SRR with horn antenna	$\lvert S_{11}\rvert$ and f_R	2.90 GHz	9.3	-	1-2 MHz/ε_R	-
[20]	No	SRs and TL	$\lvert S_{21}\rvert$ and f_R	1.50 GHz	13.0	218	-	2.90% of ε_r
T.W.	No	Planar SR	$\mathbb{R}e\{Z_{in}\}$ and f_R	648 MHz	19.8	391	378.47 Ω/mm	0.1% of V_0

V. CONCLUSION

In this article, a novel microwave contactless sensor based on the dielectric contrast with a millimetric resolution has been investigated. The implemented detection system comprises an internal SR sensitive to the target composition variation, and a probe loop required for both power supply and output signal reading. The overall hardware system works at 648 MHz. The operating principle of the sensor was analytically described and demonstrated using the equivalent RLC circuit model and the Maxwell–Garnett formula. The design was achieved by following a Q-factor optimization procedure, to maximize the sensitivity of the proposed system.

In particular, the inclusion detection and monitoring are achieved by recording the system parameter variations which are dependent on the inclusion dielectric properties, size, and location. Once an inclusion is present, an operating frequency shift and an amplitude variation of the probe loop input impedance can be accordingly observed. The improved sensitivity of the system allows to effectively detect millimeter inclusions in the investigated region. The sensor performance has been evaluated both numerically and experimentally, finding good agreement.

While the developed sensing system has been specifically suggested in this work for the detection of air bubbles during a hemodialysis treatment, the proposed sensor is an excellent candidate for every electronic device (biological, medical, industrial, and other applications) where fine target detection is a key aspect. Likewise, the proposed sensor is a compact, cost-effective, and easy-to-integrate solution.

In summary, the obtained preliminary results confirmed the theoretical approach and encourage future work. Definitely, one of the main goals is to use this technology to improve safety and lead to less invasive and more effective biomedical treatments.

REFERENCES

[1] H. Wan et al., "Biomedical sensors," in *Biomedical Information Technology*. Amsterdam, The Netherlands: Elsevier, 2020, pp. 51–79, doi: 10.1016/B978-0-12-816034-3.00002-X.

[2] A. J. Healey, P. Fathi, and N. C. Karmakar, "RFID sensors in medical applications," *IEEE J. Radio Freq. Identificat.*, vol. 4, no. 3, pp. 212–221, Sep. 2020, doi: 10.1109/JRFID.2020.2997708.

[3] G. Zhou, Y. Wang, and L. Cui, "Biomedical sensor, device and measurement systems," in *Advances in Bioengineering*. Rijeka, Croatia: InTech, 2015, doi: 10.5772/59941.

[4] V. Naresh and N. Lee, "A review on biosensors and recent development of nanostructured materials-enabled biosensors," *Sensors*, vol. 21, no. 4, pp. 1–35, Feb. 2021, doi: 10.3390/s21041109.

[5] U. Forsberg, P. Jonsson, C. Stegmayr, and B. Stegmayr, "A high blood level in the air trap reduces microemboli during hemodialysis," *Artif. Organs*, vol. 36, no. 6, pp. 525–529, Jun. 2012, doi: 10.1111/j.1525-1594.2011.01415.x.

[6] M. A. Mirski, A. V. Lele, L. Fitzsimmons, T. J. K. Toung, and D. C. Warltier, "Diagnosis and treatment of vascular air embolism," *Anesthesiology*, vol. 106, no. 1, pp. 164–177, Jan. 2007, doi: 10.1097/00000542-200701000-00026.

[7] N. Malik et al., "Air embolism: Diagnosis and management," *Future Cardiol.*, vol. 13, no. 4, pp. 365–378, Jul. 2017, doi: 10.2217/fca-2017-0015.

[8] J. K. M. Alves, D. M. A. Carvalho, S. C. Oliveira, and R. Cassia-Moura, "Bubbles and clots optical sensor prototype: A system for use in hemodialysis," in *IEEE MTT-S Int. Microw. Symp. Dig.* Piscataway, NJ, USA: Institute of Electrical and Electronics Engineers, Nov. 2015, pp. 1–3, doi: 10.1109/IMOC.2015.7369221.

[9] B. Stegmayr, "Air contamination during hemodialysis should be minimized," *Hemodialysis Int.*, vol. 21, no. 2, pp. 168–172, Apr. 2017, doi: 10.1111/hdi.12474.

[10] P. R. Keshaviah and S. Shaldon, "Hemodialysis monitors and monitoring," in *Replacement of Renal Function by Dialysis*. Dordrecht, The Netherlands: Springer, 1989, pp. 276–299, doi: 10.1007/978-94-009-1087-4_12.

[11] M. G. A. Ahmed, A. B. Adam, J. O. Dennis, and G. S. Steele, "Capacitor device for air bubbles monitoring," *Int. J. Electr. Comput. Sci.*, vol. 9, no. 10, pp. 12–15, 2009.

[12] M. G. Abdalrahman, A. B. Adam, and J. O. Dennis, "Capacitive air bubble detector for moving blood in artificial kidney," in *Proc. 3rd Int. Symp. Biomed. Eng.*, 2009, pp. 332–337.

[13] N. D. Hai, P. H. Nam, V. Q. Tuan, T. T. T. Ha, N. N. Minh, and C. D. Trinh, "Air bubbles detection and alarm in the blood stream of dialysis using capacitive sensors," in *Proc. Int. Conf. Eng. Mech. Automat. (ICEMA)*, Hanoi, Vietnam, Oct. 2014, pp. 1–6.

[14] P. Busono, "Development of ultrasonic based air bubble detection and safety system for hemodialysis machine to prevent embolism," *Appl. Mech. Mater.*, vol. 771, pp. 116–120, Jul. 2015, doi: 10.4028/www.scientific.net/amm.771.116.

[15] C. Steinem and A. Janshoff, *Piezoelectric Sensors*, vol. 5. Berlin, Germany: Springer, 2007.

[16] J. D. Pittard, "Safety monitors in hemodialysis," in *Handbook of Dialysis Therapy*. Amsterdam, The Netherlands: Elsevier, 2023, pp. 101–117, doi: 10.1016/B978-0-323-79135-9.00009-4.

[17] W. Wang et al., "MRC-based double figure-of-eight coil sensor system with triple-mode operation capability for biomedical applications," *IEEE Sensors J.*, vol. 21, no. 13, pp. 14491–14502, Jul. 2021, doi: 10.1109/JSEN.2020.3020578.

[18] W. Wang et al., "Wideband gain enhancement of MIMO antenna and its application in FMCW radar sensor integrated with CMOS-based transceiver chip for human respiratory monitoring," *IEEE Trans. Antennas Propag.*, vol. 71, no. 1, pp. 318–329, Jan. 2023, doi: 10.1109/TAP.2022.3222802.

[19] N. AlSawaftah, S. El-Abed, S. Dhou, and A. Zakaria, "Microwave imaging for early breast cancer detection: Current state, challenges, and future directions," *J. Imag.*, vol. 8, no. 5, p. 123, Apr. 2022, doi: 10.3390/jimaging8050123.

[20] X. Wang, H. Deng, and C. Liu, "High-Q sensor for permittivity detection based on spiral resonator," *Appl. Phys. A, Mater. Sci. Process.*, vol. 124, no. 11, pp. 1–8, Nov. 2018, doi: 10.1007/s00339-018-2152-x.

[21] D. Yang and Y. Dong, "Miniaturized multilayer surface-mountable 5G filter based on shielded spiral resonator," *IEEE Trans. Circuits Syst. II, Exp. Briefs*, vol. 69, no. 8, pp. 3366–3370, Aug. 2022, doi: 10.1109/TCSII.2022.3168613.

[22] D. Kajfez, "Q-factor," in *Encyclopedia of RF and Microwave Engineering*. Hoboken, NJ, USA: Wiley, 2005, doi: 10.1002/0471654507.eme333.

[23] D. Brizi, J. P. Stang, A. Monorchio, and G. Lazzi, "On the design of planar arrays of nonresonant coils for tunable wireless power transfer applications," *IEEE Trans. Microw. Theory Techn.*, vol. 68, no. 9, pp. 3814–3822, Sep. 2020, doi: 10.1109/TMTT.2020.2983145.

[24] M. W. Knight, N. S. King, L. Liu, H. O. Everitt, P. Nordlander, and N. J. Halas, "Aluminum for plasmonics," *ACS Nano*, vol. 8, no. 1, pp. 834–840, Jan. 2014, doi: 10.1021/nn405495q.

[25] D. Courjon and C. Bainier, "Near field microscopy and near field optics," *Rep. Prog. Phys.*, vol. 57, no. 10, pp. 989–1028, Oct. 1994, doi: 10.1088/0034-4885/57/10/002.

[26] F. Bilotti, A. Toscano, L. Vegni, K. Aydin, K. B. Alici, and E. Ozbay, "Equivalent-circuit models for the design of metamaterials based on artificial magnetic inclusions," *IEEE Trans. Microw. Theory Techn.*, vol. 55, no. 12, pp. 2865–2873, Dec. 2007, doi: 10.1109/TMTT.2007.909611.

[27] G. A. Lee, M. A. Megahed, and F. de Flaviis, "Low-cost compact spiral inductor resonator filters for system-in-a-package," *IEEE Trans. Adv. Packag.*, vol. 28, no. 4, pp. 761–771, Nov. 2005, doi: 10.1109/TADVP.2005.850504.

[28] D. Brizi, N. Fontana, F. Costa, and A. Monorchio, "Accurate extraction of equivalent circuit parameters of spiral resonators for the design of metamaterials," *IEEE Trans. Microw. Theory Techn.*, vol. 67, no. 2, pp. 626–633, Feb. 2019, doi: 10.1109/TMTT.2018.2883036.

[29] A. Olivei, "Optimized miniature thin-film planar inductors, compatible with integrated circuits," *IEEE Trans. Parts, Mater., Packag.*, vol. PMP-5, no. 2, pp. 71–88, Jun. 1969, doi: 10.1109/TPMP.1969.1136062.

[30] D. Brizi and A. Monorchio, "Magnetic metasurfaces properties in the near field regions," *Sci. Rep.*, vol. 12, no. 1, p. 3258, Feb. 2022, doi: 10.1038/s41598-022-07378-y.

[31] A. V. Vorst, A. Rosen, and Y. Kotsuka, "RF/microwave interaction mechanisms in biological materials," in *RF/Microwave Interaction With Biological Tissues*. Hoboken, NJ, USA: Wiley, 2006, pp. 63–91.

[32] D. Formica and S. Silvestri, "Biological effects of exposure to magnetic resonance imaging: An overview," *Biomed. Eng. OnLine*, vol. 3, no. 1, p. 11, Dec. 2004, doi: 10.1186/1475-925X-3-11.

[33] F. A. Duck, *Physical Properties of Tissues: A Comprehensive Reference Book*. New York, NY, USA: Academic, 2013.

[34] W. Kuang and S. O. Nelson, "Low-frequency dielectric properties of biological tissues: A review with some new insights," *Trans. ASAE*, vol. 41, no. 1, pp. 173–184, 1998.

[35] C. Gabriel, S. Gabriel, and E. Corthout, "The dielectric properties of biological tissues: I. Literature survey," *Phys. Med. Biol.*, vol. 41, no. 11, pp. 2231–2249, Nov. 1996, doi: 10.1088/0031-9155/41/11/001.

[36] H. Griffiths, W. R. Stewart, and W. Gough, "Magnetic induction tomography: A measuring system for biological tissues," *Ann. New York Acad. Sci.*, vol. 873, no. 1, pp. 335–345, 1999.

[37] N. De Geeter, G. Crevecoeur, and L. Dupré, "Eddy-current simulations using an independent impedance method in anisotropic biological tissues," *IEEE Trans. Magn.*, vol. 47, no. 10, pp. 3845–3848, Oct. 2011, doi: 10.1109/TMAG.2011.2145361.

[38] E. A. Badea and O. Craiu, "Eddy current effects in MRI superconducting magnets," *IEEE Trans. Magn.*, vol. 33, no. 2, pp. 1330–1333, Mar. 1997, doi: 10.1109/20.582501.

[39] M. Sekino and S. Ueno, "FEM-based determination of optimum current distribution in transcranial magnetic stimulation as an alternative to electroconvulsive therapy," *IEEE Trans. Magn.*, vol. 40, no. 4, pp. 2167–2169, Jul. 2004, doi: 10.1109/TMAG.2004.828982.

[40] D. Brizi et al., "A radiating system for low-frequency highly focused hyperthermia with magnetic nanoparticles," *IEEE J. Electromagn., RF Microw. Med. Biol.*, vol. 4, no. 2, pp. 109–116, Jun. 2020, doi: 10.1109/JERM.2019.2945833.

[41] F. Costa et al., "Wireless detection of water level by using spiral resonators operating in sub-GHz range," in *Proc. IEEE Int. Conf. RFID Technol. Appl. (RFID-TA)*, Sep. 2019, pp. 197–200, doi: 10.1109/RFID-TA.2019.8892141.

[42] A. H. Sihvola, "Mixing rules with complex dielectric coefficients," *Subsurface Sens. Technol. Appl.*, vol. 1, no. 4, pp. 393–415, Oct. 2000, doi: 10.1023/A:1026511515005.

[43] R. Balduino et al., "Feasibility of water content-based dielectric characterisation of biological tissues using mixture models," *IEEE Trans. Dielectr. Electr. Insul.*, vol. 26, no. 1, pp. 187–193, Feb. 2019, doi: 10.1109/TDEI.2018.007412.

[44] Z. J. Davis, W. Svendsen, and A. Boisen, "Design, fabrication and testing of a novel MEMS resonator for mass sensing applications," *Microelectron. Eng.*, vol. 84, nos. 5–8, pp. 1601–1605, May 2007, doi: 10.1016/j.mee.2007.01.199.

[45] W.-Y. Yin, S. J. Pan, L.-W. Li, Y.-B. Gan, and F. Lin, "Local scalable description of global characteristics of various on-chip asymmetrically octagonal inductors," *IEEE Trans. Magn.*, vol. 39, no. 4, pp. 2042–2048, Jul. 2003, doi: 10.1109/TMAG.2003.814292.

[46] A. H. Sarhadi, A. Hashemi, and H. Emami, "Optimization of Q factor in complementary spiral resonator for RFID application," in *Proc. 21st Telecommun. Forum Telfor (TELFOR)*, Nov. 2013, pp. 693–696, doi: 10.1109/TELFOR.2013.6716323.

[47] P. Sergienko, V. Kazmirenko, A. Chernov, and Y. Prokopenko, "Q-factor of tuned microstrip resonator," *Radioelectron. Commun. Syst.*, vol. 59, no. 2, pp. 89–95, Feb. 2016, doi: 10.3103/S0735272716020060.

[48] B. S. Virdee and C. Grassopoulos, "Folded microstrip resonator," in *IEEE MTT-S Int. Microw. Symp. Dig.*, Jun. 2003, pp. 2161–2164, doi: 10.1109/mwsym.2003.1210591.

[49] M. Amin, R. Ramzan, and O. Siddiqui, "Slow wave applications of electromagnetically induced transparency in microstrip resonator," *Sci. Rep.*, vol. 8, no. 1, p. 2357, Feb. 2018, doi: 10.1038/s41598-018-20771-w.

[50] D. Moschou and A. Tserepi, "The lab-on-PCB approach: Tackling the μTAS commercial upscaling bottleneck," *Lab Chip*, vol. 17, no. 8, pp. 1388–1405, Apr. 2017, doi: 10.1039/c7lc00121e.

[51] A. Masi, S. Rotundo, E. Canicatti, F. Molesti, D. Brizi, and A. Monorchio, "Microwave and contactless sensor for millimeter inclusions detection in biomedical applications," in *Proc. 16th Eur. Conf. Antennas Propag. (EuCAP)*, Mar. 2022, pp. 1–3, doi: 10.23919/EuCAP53622.2022.9769043.

[52] S. Lezhnin, D. Eskin, Y. Leonenko, and O. Vinogradov, "Dissolution of air bubbles in a turbulent water pipeline flow," *Heat Mass Transf.*, vol. 39, no. 5, pp. 483–487, Jun. 2003, doi: 10.1007/s00231-002-0313-z.

[53] S. Sirivithayapakorn and A. Keller, "Transport of colloids in unsaturated porous media: A pore-scale observation of processes during the dissolution of air-water interface," *Water Resour. Res.*, vol. 39, no. 12, p. 1346, Dec. 2003, doi: 10.1029/2003WR002487.

[54] J. M. Felicio, C. A. Fernandes, and J. R. Costa, "Complex permittivity and anisotropy measurement of 3D-printed PLA at microwaves and millimeter-waves," in *Proc. 22nd Int. Conf. Appl. Electromagn. Commun. (ICECOM)*. Piscataway, NJ, USA: Institute of Electrical and Electronics Engineers, Sep. 2016, pp. 1–6, doi: 10.1109/ICECom.2016.7843900.

[55] N. Kazemi, N. Gholizadeh, and P. Musilek, "Selective microwave zeroth-order resonator sensor aided by machine learning," *Sensors*, vol. 22, no. 14, p. 5362, Jul. 2022, doi: 10.3390/s22145362.

[56] M. Abdolrazzaghi, M. H. Zarifi, W. Pedrycz, and M. Daneshmand, "Robust ultra-high resolution microwave planar sensor using fuzzy neural network approach," *IEEE Sensors J.*, vol. 17, no. 2, pp. 323–332, Jan. 2017, doi: 10.1109/JSEN.2016.2631618.

[57] M. A. Mahmoud, G. R. Henderson, E. K. Epprecht, and W. H. Woodall, "Estimating the standard deviation in quality-control applications," *J. Qual. Technol.*, vol. 42, no. 4, pp. 348–357, Oct. 2010, doi: 10.1080/00224065.2010.11917832.

[58] B. A. Walther and J. L. Moore, "The concepts of bias, precision and accuracy, and their use in testing the performance of species richness estimators, with a literature review of estimator performance," *Ecography*, vol. 28, no. 6, pp. 815–829, Dec. 2005, doi: 10.1111/j.2005.0906-7590.04112.x.

[59] M. Kanso, S. Cuenot, and G. Louarn, "Sensitivity of optical fiber sensor based on surface plasmon resonance: Modeling and experiments," *Plasmonics*, vol. 3, nos. 2–3, pp. 49–57, Sep. 2008, doi: 10.1007/s11468-008-9055-1.

[60] Z. Abbasi, H. Niazi, M. Abdolrazzaghi, W. Chen, and M. Daneshmand, "Monitoring pH level using high-resolution microwave sensor for mitigation of stress corrosion cracking in steel pipelines," *IEEE Sensors J.*, vol. 20, no. 13, pp. 7033–7043, Jul. 2020, doi: 10.1109/JSEN.2020.2978086.

[61] M. H. Zarifi, T. Thundat, and M. Daneshmand, "High resolution microwave microstrip resonator for sensing applications," *Sens. Actuators A Phys.*, vol. 233, pp. 224–230, Sep. 2015, doi: 10.1016/j.sna.2015.06.031.

[62] A. Soltan, R. A. Sadeghzadeh, and S. Mohammad-Ali-Nezhad, "Microwave sensor for liquid classification and permittivity estimation of dielectric materials," *Sens. Actuators A, Phys.*, vol. 336, Apr. 2022, Art. no. 113397, doi: 10.1016/j.sna.2022.113397.

[63] Z. Qiu et al., "A metamaterial based microfluidic sensor for permittivity detection of liquid," *J. Phys. D, Appl. Phys.*, vol. 55, no. 43, Oct. 2022, Art. no. 435001, doi: 10.1088/1361-6463/ac893e.

[64] B. D. Wiltshire, T. Zarifi, and M. H. Zarifi, "Passive split ring resonator tag configuration for RFID-based wireless permittivity sensing," *IEEE Sensors J.*, vol. 20, no. 4, pp. 1904–1911, Feb. 2020, doi: 10.1109/JSEN.2019.2950912.

Angelica Masi (Graduate Student Member, IEEE) was born in Prato, Italy, in 1995. She received the M.S. Laurea (summa cum laude) degree in biomedical engineering from the University of Pisa, Pisa, Italy, in 2021, where she is currently pursuing the Ph.D. degree in information engineering with the Microwave and Radiation Laboratory, Department of Information Engineering.

Her research interests include the design of radio frequency and microwave sensors, metasurfaces for biosensing applications, dielectric characterization of solids and liquids, defect detection, and so on.

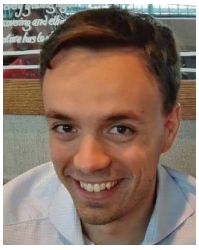

Danilo Brizi (Member, IEEE) was born in Viterbo, Italy, in 1992. He received the M.S. Laurea (summa cum laude) degree in biomedical engineering and the Ph.D. (summa cum laude) degree in information engineering from the University of Pisa, Pisa, Italy, in 2016 and 2020, respectively.

He is currently an Assistant Professor with the University of Pisa. His research interests include electromagnetic metasurfaces, magnetic resonance imaging (MRI) filter design, and wireless power transfer applications.

Dr. Brizi serves as a Reviewer for international journals, and he is an Associate Editor of *IEEE Antennas and Propagation Magazine*, since 2022.

Agostino Monorchio (Fellow, IEEE) is a Full Professor with the University of Pisa, Pisa, Italy. He spent several research periods with the Electromagnetic Communication Laboratory, Pennsylvania State University, University Park, PA, USA. He has carried out considerable research activity and technical consultancy to national, European Union (EU), and U.S. industries, coordinating, as a Principal Scientific Investigator, a large number of national and European research projects. The activity is mainly carried out at the Microwave and Radiation Laboratory (www.mrlab.it), Department of Information Engineering, University of Pisa, together with a large group of Ph.D. students, postdoctoral researchers, and research associates. He is the Head of RaSS National Laboratory, Consorzio Nazionale Interuniversitario per le Telecomunicazioni (CNIT), Pisa. In 2012, his contributions to computational electromagnetics and for application of frequency selective surfaces in metamaterials. His research results have been published in more than 170 journal articles and book chapters, and more than 260 communications at international and national conferences. He is a coauthor of four patents. Prof. Monorchio is active in a number of areas including computational electromagnetics, microwave metamaterials, radio propagation for wireless systems, the design and miniaturization of antennas and electromagnetic compatibility, and biomedical microwave applications.

Prof. Monorchio is a member of the Scientific Advisory Board of the Directed Energy Research Center of TII (Abu Dhabi, United Arab Emirates) and affiliated with the Pisa Section of Istituto Nazionale di Fisica Nucleare (INFN), the National Institute of Nuclear Physics. He has been an AdCom Member from 2017 to 2019 and he is the Co-Chair of the Industrial Initiative Committee of the IEEE Antennas and Propagation Society (APS). He was a recipient of the Scholarship (Fellowship Award) of the Summa Foundation, New Mexico (USA), and in the framework of the CNR-NATO Senior Fellowship Program. He serves as a Reviewer for international journals, and he was an Associate Editor of IEEE ANTENNAS AND WIRELESS PROPAGATION LETTERS from 2002 to 2007.

Open Access funding provided by 'Università di Pisa' within the CRUI CARE Agreement